THE JOURNAL OF PHYSICAL CHEMISTRY C
A JOURNAL OF THE AMERICAN CHEMICAL SOCIETY

pubs.acs.org/JPCC Article

Transient On/Off Photocurrent Response of Halide Perovskite Photodetectors

Published as part of The Journal of Physical Chemistry C virtual special issue "The Physical Chemistry of Perovskites".

Juan Bisquert,* Cedric Gonzales, and Antonio Guerrero

Cite This: *J. Phys. Chem. C* 2023, 127, 21338−21350 Read Online

ACCESS | Metrics & More | Article Recommendations

ABSTRACT: Solution-processed photodetectors such as those based on halide perovskite semiconductors show attractive properties for emerging applications in lightweight, transparent, flexible, and spectrally selective optical sensors. The transient photocurrent to a light perturbation often shows a complex response characterized by sharp transient peaks in the photocurrent curves when the stimulus changes or slow rise times depending on features such as the applied voltage or the active layer thickness. We present the characteristic response of halide perovskite photodetectors by measuring the response of a FTO/PEDOT/$MAPbBr_3$/Au device, and we establish a new model for the analysis of the dominant transient shapes. The model uses very basic suppositions of photoconversion to electricity: charge generation, collection, and polarization. These standard properties are combined with a new essential feature: a delayed photocurrent mode that forms a photoinduced chemical inductor. This last property is caused by ionic−electronic interaction phenomena related to the well-known inverted hysteresis of perovskite devices. We show that these elementary properties explain well the varied characteristic time transient currents in on/off voltages and light switching.

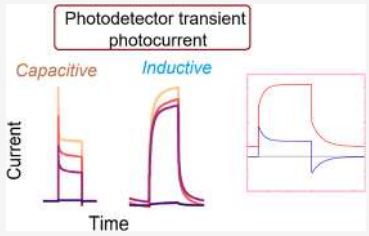

1. INTRODUCTION

The photodetector (PD) is a device that converts a light perturbation into an electrical signal. PDs serve as essential components in various commercial and scientific applications encompassing imaging, optical fiber communications, spectroscopy, and biomedical fields. The existing PDs available in the market predominantly employ inorganic semiconductor materials such as Si and InGaAs for ultraviolet, visible, and infrared detection. Another class of materials is the solution-processed semiconductors that include organic materials, metal halide perovskites, and inorganic nanocrystals and quantum dots.[1] The demand for lightweight, transparent, flexible, and spectrally selective optical sensors has emerged. Addressing this need, solution-processed semiconductors have garnered significant attention due to their unique photoelectric characteristics, including high light absorption coefficients in the visible range, adaptability of the optical bandgaps for spectral selection, and excellent carrier transport, among others.[1−9]

In this article, we present a new approach for the interpretation and characterization of transient photocurrent responses of solution-processed PDs under light on/off switching. By examining these properties, we aim to provide a new important tool in the development of next-generation PDs for the rapid advancement of emerging applications such as lightweight portable devices and retinomorphic event-based cameras.

Two-contact PD devices are formed by an active photoconductor layer where incident light produces excited charge carriers, combined with contact layers that may range from simple metal electrodes to layered charge-selective contacts that enhance charge collection and impart directionality to the photocurrent.[5] The transient response of a PD in the on/off cycles of a square light pulse is a central characteristic of the quality of operation of the device and for discriminating different light levels. Ideally, a fully flat current response is required, but measurements made over many years with silicon, organic, and perovskite PDs show a number of distinct characteristics.[10,11] In addition, the detection behavior of perovskite PDs exhibits temporal variations and current drift. These features often result in significant challenges in the characterization of device performance.[12−15]

Representative shapes of the transient photocurrent in response to a light pulse are shown in Figures 1 and 2 for devices based on halide perovskite materials. In Figure 1A, it is observed that the shape of the transient changes when the

Received: July 11, 2023
Revised: August 23, 2023
Published: October 19, 2023

Downloaded via UNIV JAUME I on November 8, 2023 at 12:33:22 (UTC).
See https://pubs.acs.org/sharingguidelines for options on how to legitimately share published articles.

ACS Publications © 2023 American Chemical Society

https://doi.org/10.1021/acs.jpcc.3c04672
J. Phys. Chem. C 2023, 127, 21338−21350

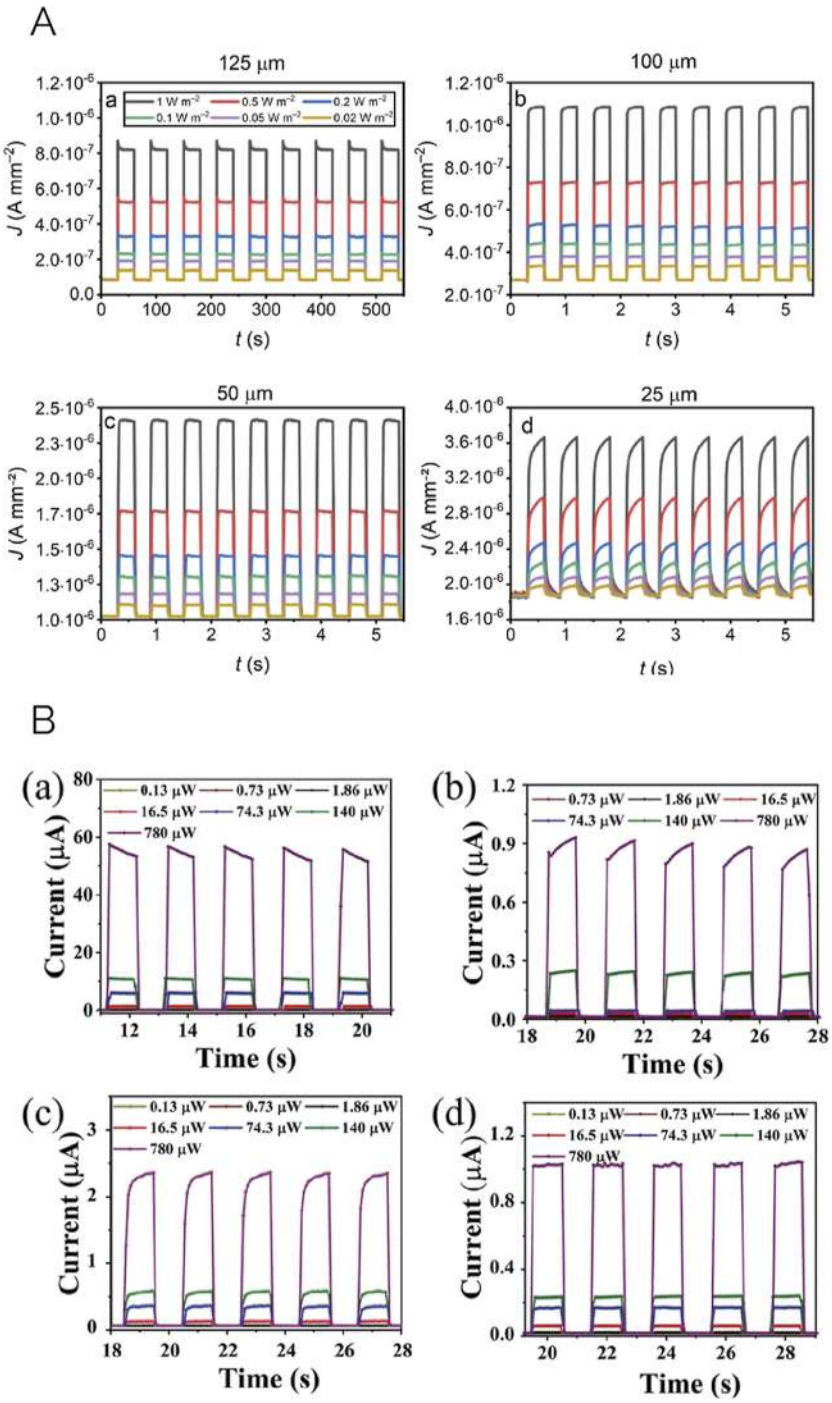

Figure 1. (A) Transient photocurrent responses of methylammonium lead bromide devices measured at a fixed bias voltage of 2 V under 576 nm visible illumination with different light intensities ranging from 1 to 0.02 W m^{-2}. Reprinted with permission from Gavranovic, S.; Pospisil, J.; Zmeskal, O.; Novak, V.; Vanysek, P.; Castkova, K.; Cihlar, J.; Weiter, M., *ACS Appl. Mater. Interfaces* **2022**, 14, 20159−20167. Copyright 2022 American Chemical Society. (B) Photoresponse of four mixed-halide perovskite single-crystal PDs. The illumination power varied from 0.13 to 780 μW. Reprinted with permission from Ding, J.; Gao, W.; Gao, L.; Lu, K.; Liu, Y.; Sun, J.-L. and Yan, Q. Unraveling the Effect of Halogen Ion Substitution on the Noise of a Perovskite Single-Crystal PD, *J. Phys. Chem. Lett.* **2022**, 13, 7831−7837. Copyright 2022 American Chemical Society.

channel length of a lateral perovskite PD is decreased.[16] The ideal flat current response is observed in some cases. But there are more structured typical shapes in which an initial spike is observed or stabilization of the current is slow, as shown in Figure 1B.[17]

In the case of the long channel device, Figure 1A(a), an initial peak occurs that exceeds the stabilized current level. The initial overshoot phenomenon, wherein sharp transient peaks in the photocurrent curves occur when the incident light signal changes rapidly, Figure 2A,[18] is a widely observed feature that complicates the detection of the signal of the PD, as observed in the long transient decay of Figure 2B.[19,20] This feature is usually attributed to charge accumulation phenomena, and different models have been presented combining carrier

https://doi.org/10.1021/acs.jpcc.3c04672
J. Phys. Chem. C 2023, 127, 21338−21350

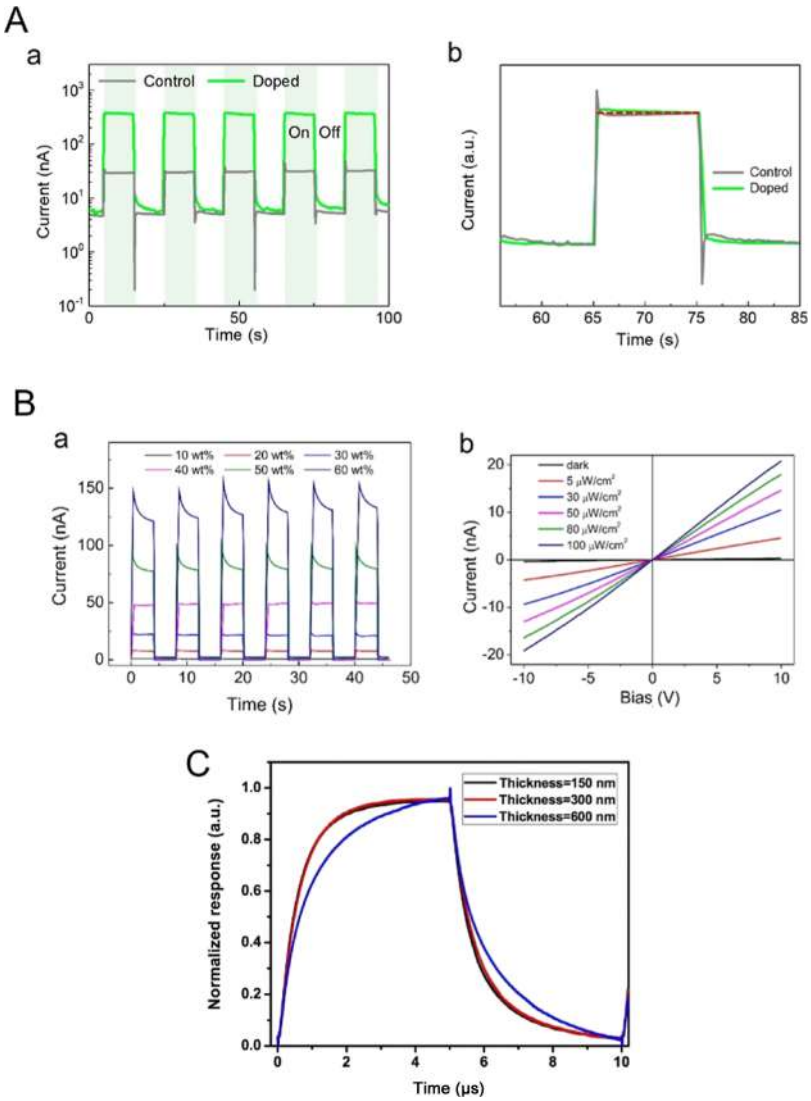

Figure 2. (A) (a) Transient time current curves of a perovskite nanocrystal-based PD and (b) normalized transient current curves of a control and doped nanocrystal-based PDs, respectively. Reproduced from Wang, T.; Fang, T.; Li, X.; Xu, L.; Song, J., J. Phys. Chem. C 2021, 125, 5475−5484. Copyright 2022 American Chemical Society. (B) (a) $I-t$ curves of network PD arrays of methylammonium lead iodide perovskite with different precursor concentrations. The bias voltage was 10 V, and the 650 nm light power density was 100 μW/cm^2. (b) $I-V$ curves under different illumination power densities at a bias voltage of 10 V for 30 wt % precursor concentration. Reproduced with permission from Deng, H.; Yang, X.; Dong, D.; Li, B.; Yang, D.; Yuan, S.; Qiao, K.; Cheng, Y.-B.; Tang, J.; Song, H., Nano Lett. 2015, 15, 7963−7969. Copyright 2015 American Chemical Society. (C) Temporal response of perovskite PDs of different thicknesses. Reproduced from Dou, L.; Yang, Y.; You, J.; Hong, Z.; Chang, W.-H.; Li, G.; Yang, Y., Nat. Commun. 2014, 5, 5404, licensed under a Creative Commons Attribution (CC BY) license.

generation, extraction, recombination, and trap-related phenomena.[3,10,21]

In the case of the short channel devices in the lateral configuration, Figure 1A(d), the peak is replaced by a contrary pattern in which the current first increases abruptly and then rises further slowly with time.[22,23] A rise time and fall time of the photocurrent intensity are often used to characterize the response speed of the PD to the optical signal. It has been observed that the rise time increases with the film thickness. In Figure 2C, another pattern is shown where the current increases slowly from the first instant.[12,23] These responses have been recognized from early measurements of perovskite PDs[13,24] and attributed to the large capacitance present in the devices. These problems of the slow rise of the photocurrent persist in current perovskite PDs.[8,14,15] The different types of features, peak, fast−slow rise, and slow rise, have been amply reported in different types of PDs.[3,15,16,20,25−27]

This paper presents an analysis of the impact of voltage and illumination perturbations on a lead halide perovskite PD. We focus on investigating the pure photoelectrical characteristics of the sample, which play a crucial role in determining its transient response. By incorporating a minimal model, we aim to provide an explanation for the various types of transients observed, drawing on the prominent feature of a chemical inductor commonly observed in halide perovskite samples.[28−31] This phenomenon arises from the mixed ionic−electronic conduction in these materials, and our model is further supported by recent findings in halide perovskite solar cells and memristors.[28,30−34]

Through our study, we introduce the first model of a photoconductor with a delayed response and demonstrate how

https://doi.org/10.1021/acs.jpcc.3c04672
J. Phys. Chem. C 2023, 127, 21338−21350

the transient photocurrent signatures can account for the experimental observations typically reported in the literature for solution-processed PDs, as illustrated in Figures 1 and 2.

In Section 2, we describe the materials and methods of measurement. Section 3 presents the model for the transient responses. Section 4 reports the results of the measurements on a methylammonium lead bromide ($MAPbBr_3$) device. Section 5 analyzes, first, the response to a voltage step and then the transient in response to a square light pulse. We discuss the interpretation of the normally observed response in terms of the model, and we finish with some conclusions.

2. METHODS

2.1. Device Preparation. The fluorine-doped tin oxide (FTO) substrates (TEC15) were partially etched with zinc powder and a 2 M hydrochloric acid solution. The etched samples were individually brushed to mechanically remove residues from the etching process. The brushed samples were then subjected to a sequency of 15 min sonication in deionized water with Hellmanex detergent solution, acetone, and isopropyl alcohol. The cleaned samples were blow-dried by using a nitrogen gun.

Prior to the deposition of the poly(3,4-ethylenedioxythiophene) polystyrenesulfonate (PEDOT:PSS), the cleaned samples were subjected to an ultraviolet−ozone (UV−O_3) treatment for 15 min to further remove organic contamination on the surface and improve the surface wetting. The PEDOT:PSS solution (Clevios P VP. Al 4083) was filtered using a 0.45 μm Nylon filter and was statically spin-coated onto the etched FTO substrates for 30 s at 3000 rpm with an acceleration of 1000 rpm/s. The deposited PEDOT:PSS was annealed at 100 °C for 5 min and then immediately transported into a nitrogen-controlled glovebox in preparation for the $MAPbBr_3$ perovskite deposition.

A 1.4 M $MAPbBr_3$ precursor solution was prepared using $PbBr_2$ (>98%, TCI) and MABr (>99.99%, Greatcell Solar) in a 1:4 dimethyl sulfoxide (DMSO) (≥99.9%, Sigma-Aldrich): *N*,*N*-dimethylformamide (DMF) (99.8%, Sigma-Aldrich) solution. A 50 μL $MAPbBr_3$ perovskite solution was statically spin-coated onto the PEDOT:PSS layer via a two-step antisolvent method: 10 s at 1000 rpm, followed by 40 s at 4000 rpm. A 400 μL toluene (99.8%, Sigma-Aldrich) antisolvent was injected 32 s before the spin coating ended. The samples were then annealed at 100 °C for 30 min.

Finally, an 85 nm gold contact was thermally evaporated by using a commercial Oerlikon Leybold Univex 250.

2.2. Voltage-Dependent Transient Current Response. The characteristic $I-V$ curves of the perovskite devices were measured inside a nitrogen-controlled glovebox under dark conditions using an Autolab PGSTAT204 with a scan rate of 1 V/s. The transient current response of the device at applied voltage (V_{app}) pulses was measured using 20 voltage pulses with a pulse width (t_{app}) of 10 ms. The V_{app} was varied from 0.2 to 1.6 V at a voltage interval of 0.2 V.

2.3. Illumination Intensity-Dependent Transient Photocurrent Response. The characteristic $I-V$ curves of the perovskite devices with varying illumination intensities were measured using an Autolab PGSTAT30 and Xenon white light source (USHIO UXL-150MO) with an irradiance of 100 mW cm^{-2} (1 Sun) under ambient conditions. The illumination intensity was varied using neutral density filters with optical densities (ODs) of 0.1, 0.3, and 2.0. The illumination intensity-dependent transient photocurrent response of the device at a constant V_{app} was measured using a waveform-generator-controlled mechanical shutter at a 0.2 Hz shutter frequency. The V_{app} was varied from 0 to 0.25 V at a voltage interval of 0.05 V.

3. MODEL

We developed a new model to explain the main characteristics of the transients. As mentioned in the Introduction, many authors have established models and explanations based on specific physical effects of photoexcited carriers, such as trapping, recombination, charge separation, and polarization. However, a successful classification of transient photocurrent responses has not been achieved, to the best of our knowledge, since the mentioned models are particular to the supposed physical mechanisms adopted for each situation.

Here, we take a broader view by formulating a generic model that produces the experimentally observed features in terms of some basic key physical parameters for polarization, transport, and a mechanism that introduces fast−slow-type dynamics.[35] This approach has the same spirit as a variety of neuron-style models, in which a few equations for conduction, polarization, and a short set of internal-state variables enable them to describe very complex dynamics.[36,37] We have recently developed this approach for halide perovskite solar cells and memristors,[28,30−34] and here, we add for the first time the photogeneration effects.

The key aspect we bring here, in addition to the capacitive charging and discharging and the drift transport of photogenerated carriers, is based on the idea of the chemical inductor,[28,30−34] in which, in addition to the fast current that responds to the applied voltage, an additional slow photocurrent component x occurs governed by a relaxation time τ_k.

We formulate the dynamic model of the PD response using the following set of equations

$$I_{tot} = \frac{V_{app} - u}{R_s} \tag{1}$$

$$I_{tot} = C_m \frac{du}{dt} + (g_{b0} + g_{b1}\Phi)u + \eta_{ph}\Phi + x \tag{2}$$

$$\tau_k \frac{dx}{dt} = (g_{a0} + g_{a1}\Phi)u - x \tag{3}$$

In this model, I_{tot} and V_{app} are the external current and voltage and R_s is a series resistance. The active part of the device has a voltage u. g_{b0} and g_{a0} are dark conductivities. One key element of the model is the interpretation of the delayed "slow" current x. Recent observation of the current transients in perovskite X-ray detectors indicates the ionic nature of the initial transient features.[38,39] Therefore, we assume that the ionic reorganization produces an electronic effect, in terms of charge collection or trapping, that enhances the electronic current.[40−42] This is a common explanation for the inverted hysteresis observed in perovskite devices.[43−46]

The new physics in eqs 1−3 is the influence of photogeneration on the measured current. Φ is the incident photon flux under illumination. We included two types of effects. First is the immediate charge collection of photogenerated charge with a quantum efficiency of η_{ph}. The second is that photogeneration produces a photoconductivity increase by the photosensitivity coefficients g_{b1} and g_{a1}. The charge collection is controlled by the electrical field, u/d. For

https://doi.org/10.1021/acs.jpcc.3c04672
J. Phys. Chem. C 2023, 127, 21338−21350

simplicity, the film thickness d is not written explicitly and is included in the conductance g.

The capacitive current is included in eq 2. Recent works on PDs explain the origin of the initial peak well in terms of capacitive effects. These photocharging features can be due, for example, to the separation of electron and hole distributions in organic semiconductors.[10,47−49] It is well-known that the capacitance in halide perovskite measured by impedance spectroscopy is a strong function of incident light and shows very large values.[50−52] As mentioned before, in perovskite PDs, it has been observed that the large capacitance has a predominant effect.[1,14] For simplicity, we describe the capacitive effect with a simple constant capacitor C_m that represents the low-frequency capacitance of the device. The transient dependence of the capacitance on light is ignored in the first approximation.

We define

$$R_b = \frac{1}{g_{b0} + g_{b1}\Phi} \tag{4}$$

$$R_a = \frac{1}{g_{a0} + g_{a1}\Phi} \tag{5}$$

$$R_{ab} = \left(\frac{1}{R_b} + \frac{1}{R_a}\right)^{-1} \tag{6}$$

Under applied voltage V_1 and incident flux Φ_1, the internal voltage is

$$u_1 = \frac{1}{1 + \frac{R_s}{R_{ab}}}(V_1 - R_s\eta_{ph}\Phi_1) \tag{7}$$

The steady-state current takes the form

$$I_{ss} = \frac{1}{1 + \frac{R_s}{R_{ab}}}\left(\frac{V_1}{R_s} + \eta_{ph}\Phi_1\right) \tag{8}$$

The photocurrent is plotted in Figure 3, showing the increase in photoconductivity that is the typical behavior found, for example, in Figure 2B(b).

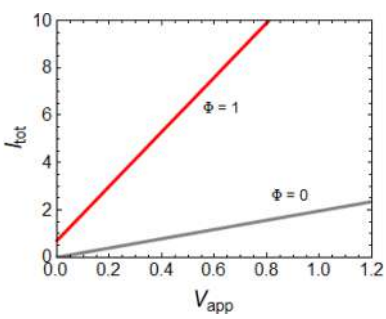

Figure 3. Current−voltage curves in the dark and under illumination. Parameters: $g_{b0} = 1$, $g_{a0} = 1$, $g_{b1} = 1$, $g_{a1} = 10$; $R_s = 0.01$, $\eta_{ph} = 0.8$.

The analysis of the small signal ac impedance gives important insight into the temporal dynamics.[28,34] The impedance of the model (1−3) is obtained by a small perturbation of voltage $\hat{V}_{app}$ to current $\hat{I}_{tot}$ at the frequency ω. Using the method explained before,[53] we find the following impedance corresponding to an equivalent circuit model in Figure 11

$$Z(\omega) = \frac{\hat{V}_{app}}{\hat{I}_{tot}} = R_s + \left[C_m i\omega + R_b^{-1} + \frac{1}{R_a + L_a i\omega}\right]^{-1} \tag{9}$$

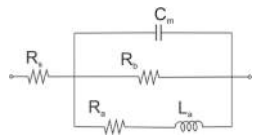

Figure 4. Equivalent circuit model.

We therefore obtain the characteristic structure of a chemical inductor[29] where the inductance element is defined as

$$L_a = R_a\tau_k \tag{10}$$

Note that the inductor is illumination-dependent. The inductive features have been reported in impedance measurements of perovskite PDs.[23] As mentioned before, the inductive process is caused by a delay in the electronic current associated with a slow ionic effect.[40−46] For a more detailed interpretation, we refer to our recent publications on the chemical inductor.[28−31]

The elements of the equivalent circuit have essential importance for the interpretation of the transient photocurrent. A preliminary scheme of several simulation results of the model is presented in Figure 5. These features will be described in detail in Section 5.

In this paper, we aim to develop a relatively simple model that explains the general trends of the transients. Each experimental system can be more complicated by different couplings of processes, morphologies, contacts, and internal voltage drops. Fortunately, one can characterize the system using impedance spectroscopy and obtain the elementary processes in order to develop the appropriate model.[54] This approach is already explained for the analysis of halide perovskite in dark conditions.[30] The effect of a nonconstant capacitance that couples to the inductor has also been described.[31]

4. RESULTS

Halide perovskite devices with the FTO/PEDOT:PSS/$MAPbBr_3$/Au configuration are fabricated as described in the Methods Section. The characteristic I−V curves in the linear and semilog scales of a representative device, measured at a scan rate of 1 V/s and under controlled conditions, are shown in Figure 6a,b, respectively. The device clearly exhibits a large inverted hysteresis typically observed in $MAPbBr_3$ solar cells and resistive switching in perovskite-based memristors, as reported in recent publications.[30,33,55]

The transient current response as a function of the applied voltage pulses is shown in Figure 6c. In this experiment, a train of square voltage pulses with amplitudes V_{app} and a pulse width (Δt) of 10 ms are applied to the device. At a low applied voltage ($V_{app} \leq 1.0$ V), the current levels are maintained throughout the sequence of voltage pulses. However, at higher applied voltage amplitudes ($V_{app} \geq 1.2$ V), the current response gradually increases with subsequent voltage pulses. This gradual increase in current response with the successive application of voltage pulses is the distinctive phenomenon of synaptic weight potentiation.[32,56] Moreover, a closer look at

https://doi.org/10.1021/acs.jpcc.3c04672
J. Phys. Chem. C 2023, 127, 21338−21350

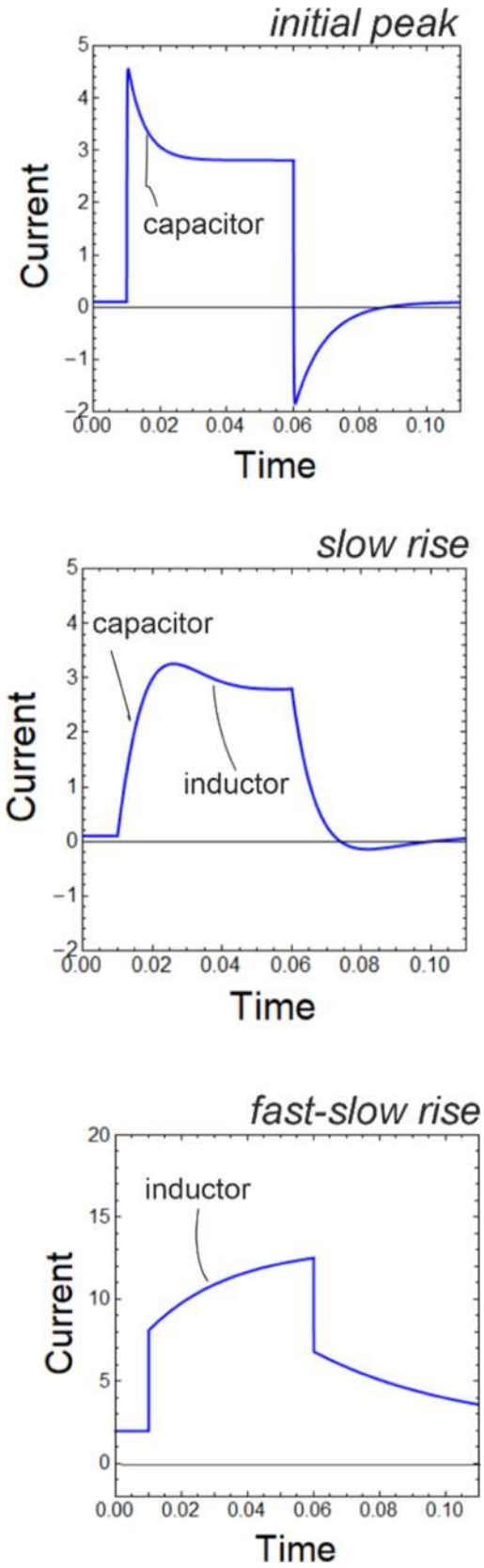

Figure 5. Scheme of the transient responses to an off/on/off cycle of illumination according to the model presented in the text. The values of capacitor, inductor, and applied voltage are different in the various panels, and the influence of each element is indicated. The examples show the main cases of transients outlined in the Introduction.

the individual transient current line shapes of representative voltages (Figure 6d) shows that an initial sharp transient peak is observed, followed by a gradual decay for low applied voltages. In contrast, at higher applied voltages, a final gradual rise in current is observed, resulting in the potentiation response of the device. This pattern has been observed in the experiments of perovskite solar cells and memristors.[28] The physical origin of the observed shapes is explained in Section 5.

On the other hand, the characteristic $I-V$ curves of the perovskite-based device measured in the dark with varying illumination intensities are shown in Figure 7a. A general increase in photocurrent is observed with increasing light intensity. Moreover, the transient photocurrent responses with varying illumination intensities measured at constant applied voltages (V_{app}) of 0 and 0.25 V are shown in Figure 7b,c, respectively. When the light is switched on at V_{app} = 0 V, the photocurrent exhibits an initial sharp transient peak, followed by a photocurrent decay at a longer time scale. In addition, when the light is switched off, there is a negative current spike followed by a fast stabilization of the current. In contrast, the transient photocurrent at V_{app} = 0.25 V exhibits a gradual increase upon illumination and a gradual decay upon removal of light. Notably, both transient photocurrent line shapes are exhibited by the same device at different measurement conditions.

In order to have a clear insight on the evolution of the photocurrent response, the transient photocurrent under on/off cycles is systematically measured with different V_{app} from 0 to 0.25 V at voltage intervals of 0.05 V. At $V_{app} \leq 0.05$ V (Figure 8a,b), the transient photocurrent exhibits an initial sharp overshoot followed by the photocurrent decay. In addition, when the light is switched off, a peak with the reverse sign of current is observed, which rapidly stabilizes. Alternatively, at V_{app} = 0.10 V (Figure 8c), after the initial overshoot, the response rapidly flattens, similar to the ideal response. Finally, at $V \geq 0.15$ V (Figure 8d−f), the photocurrent gradually increases at a faster rate with an increase in the applied voltage. The response of single pulses is compared in Figure 9 in a combined representation to have a clearer view of their evolution upon the increase in the applied voltage and light intensity. These features will be explained in Section 5 based on the model that we proposed in Section 3.

5. DISCUSSION

In the following, we apply the model to the usual experiments of on/off cycles of either voltage or illumination. We remark that the model is not restricted to these methods and can be applied to other large perturbation techniques like the photo-CELIV measurement that uses a voltage ramp.[57−59]

5.1. Voltage Transients. The electrical response of the sample is an essential property of the photocurrent response. Therefore, we first analyze the current transients in response to a voltage pulse of value V_1 and duration Δt using the insights that have been described in recent works.[28,32] The experimental transients are reported in Figure 6, and the results of our model calculations are shown in Figure 10.

Consider the initial condition, under steady illumination, Φ_1 at V_{app} = 0, that occurs before the application of the voltage step. The internal voltage has the value

$$u_0(V_{pre} = 0) = -\frac{1}{1 + \frac{R_s}{R_{ab}}} R_s \eta_{ph} \Phi_1 \tag{11}$$

https://doi.org/10.1021/acs.jpcc.3c04672
J. Phys. Chem. C 2023, 127, 21338−21350

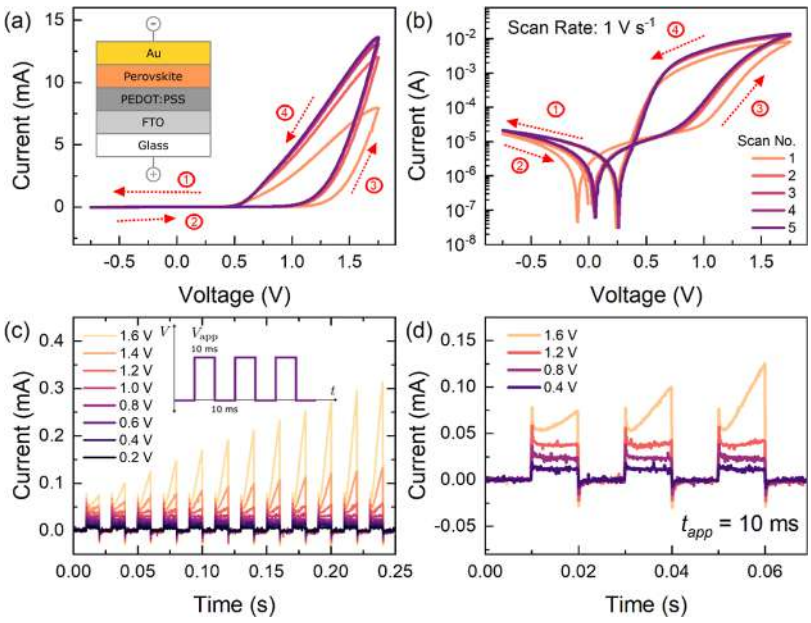

Figure 6. (a) Characteristic $I-V$ response in the linear scale of the FTO/PEDOT:PSS/$MAPbBr_3$/Au device measured in the dark with the inset illustrating the schematic diagram of the device configuration, (b) characteristic $I-V$ response of the perovskite device in the semilog scale with the arrows and numbers indicating the scan direction, (c) transient current response of the device at varying applied voltages (V_{app}) from 0.2 to 1.6 V with the inset indicating the applied voltage pulses, and (d) transient current response of the first three voltage pulses at representative applied voltages.

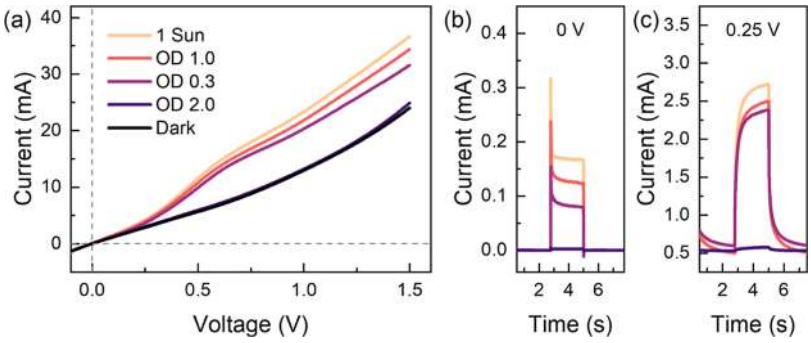

Figure 7. (a) $I-V$ curves of the perovskite device with varying illumination intensities using different optical filters, (b) transient photocurrent response with varying illumination intensities at V_{app} = 0 V exhibiting a capacitive current decay, and (c) transient photocurrent response with varying illumination intensities at V_{app} = 0.25 V exhibiting inductive charging.

Here, V_{pre} is the prestimulus value. The capacitor has a charging time

$$\tau_s = R_s C_m \tag{12}$$

When the voltage pulse V_1 is applied, initially the capacitor remains at the prestimulus level with the charge associated with the voltage in eq 11; therefore, the potential $V_1 - u_0$ occurs at the series resistance. The initial current at this moment is defined by the condition that x remains at the prepulse value, x_0.

$$x_0 = (g_{a0} + g_{a1}\Phi_1)u_0 \tag{13}$$

The corresponding current I_{in}

$$I_{in}(V_{pre} = 0) = + \frac{R_{ab}}{R_s + R_{ab}} \eta_{ph} \Phi_1 \tag{14}$$

is indicated by the green reference line in Figure 10a.

After this initial jump of the current ΔI, the capacitor starts to charge and the current decreases, as shown in the initial peak of Figure 10a. The final destination of the current I_{fi} shown by the purple line is the steady-state current of eq 8. We note in Figure 10a that the current overcomes the purple line. This is because R_a is not yet operative and the inductor L_a in Figure 4 is not activated. The current has to bend upward to reach the purple line, as shown in Figure 10b. How fast this is achieved depends on the time constant τ_k that controls the evolution of the variable x. The variable x shows an inductive behavior,[29] as commented before, implying that the current increases as time increases. If τ_k is longer than Δt as in Figure 10a, the final current is not reached. Otherwise, the current reaches the equilibrium value, as shown in Figure 10b. This increase of the current is the key property of perovskite synapses for neural networks that has already been characterized in terms of the inductive current.[32,60]

Another phenomenon occurs when the voltage pulse is finished in which the current is inverted. This is because the internal u_1 cannot change instantaneously. When the external voltage is removed, a negative voltage ($-u_1$) occurs at the series resistance, producing a negative step of the current

https://doi.org/10.1021/acs.jpcc.3c04672
J. Phys. Chem. C 2023, 127, 21338−21350

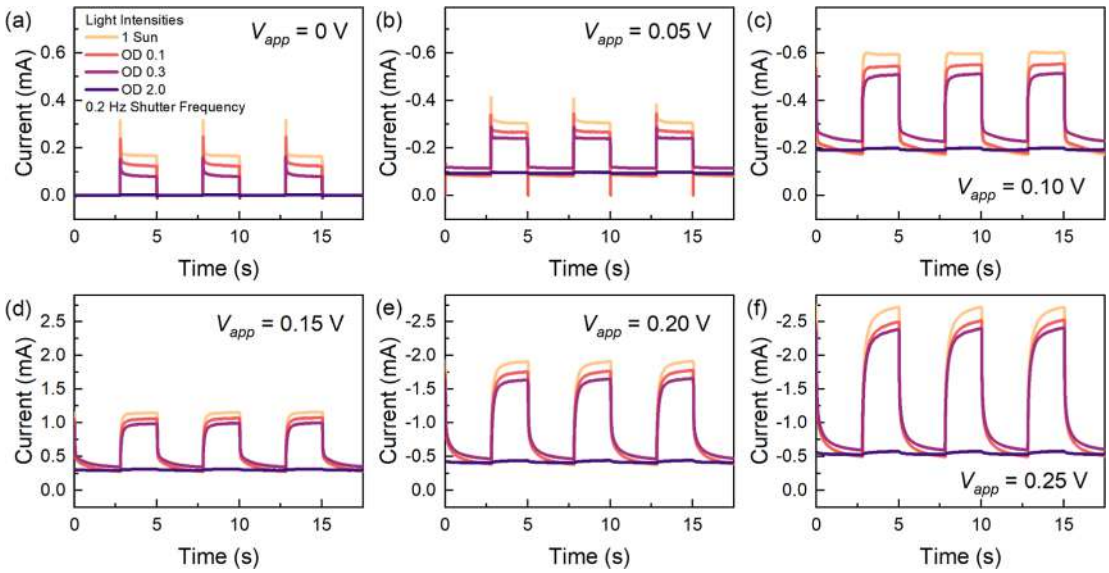

Figure 8. Illumination intensity-dependent transient photocurrent response of the perovskite device at varying V_{app} ranging from 0 to 0.25 V with a shutter frequency of 0.2 Hz.

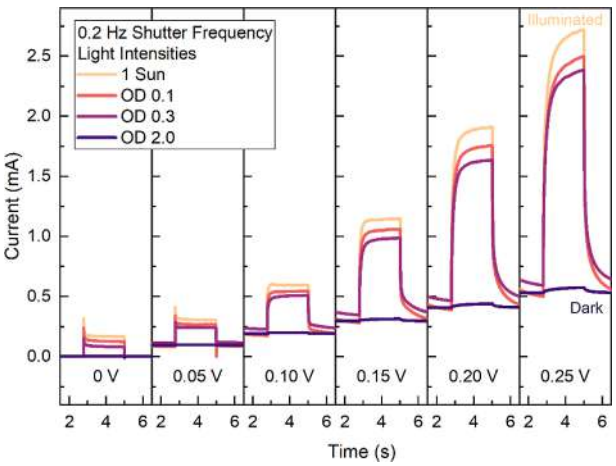

Figure 9. Illumination intensity-dependent single pulse transient photocurrent response of the perovskite device at varying V_{app} ranging from 0 to 0.25 V with a shutter frequency of 0.2 Hz.

($-\Delta I$) of the same size as the initial one. Afterward, the current returns to the initial value discharging the capacitor and deactivating the inductor.

A number of transient responses are shown in Figure 11 for diverse sets of time constants. The conclusion is that the capacitor determines the initial decline, while the inductor component controls the subsequent rise of the current, related to the potentiation effect in artificial synapses.[28,32,56]

We remark that the model responses in Figures 10 and 11 match well with the experimental observations shown in Figure 6. In the experimental transients, the following points are observed:

(i) The initial peak, due to series resistance and capacitor charging.
(ii) The subsequent current rise, and
(iii) The negative peak when the square pulse ceases.

The feature (ii) is associated with the chemical induction of this type of sample, which has been well attested in the literature.[55,61] This property is in correspondence with the

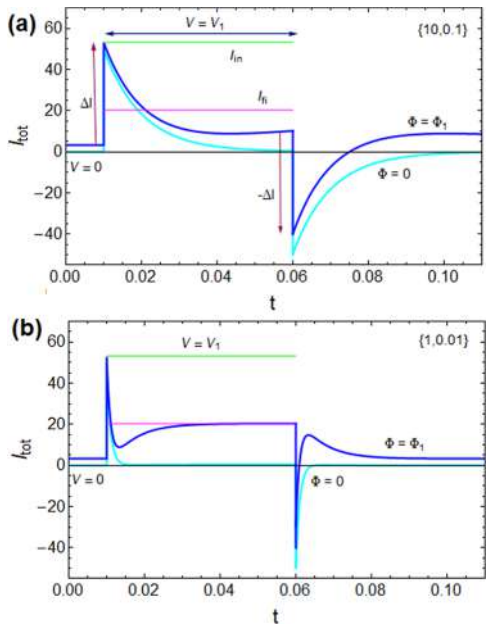

Figure 10. Model result of $I-t$ curves shows a transient voltage square pulse of value V_1 = 0.05 with duration Δt = 0.05 under constant illumination of photon flux Φ_1 = 10 (blue). The cyan line is the transient in the dark. The green and purple reference lines are the initial and final currents. Parameters: $g_{b0} = 1$, $g_{a0} = 10$, $g_{b1} = 1$, $g_{a1} = 50$; R_s = 0.001; η_{ph} = 0.5; and $\{C_m, \tau_k\}$ as indicated. Note that the capacitor charging time is $\tau_s = R_s C_m$.

large inverted hysteresis feature that is shown in Figure 6a since this type of hysteresis is associated with the inductor effect.[33,62]

5.2. Pulsed Illumination Transients. We next analyze the response of the system to a square light pulse. The characteristic results of the literature are summarized in Figures 1 and 2, and our own measurements are shown in Figures 7−9. From the experimental evidence, we conclude that there are two main types of characteristic responses, as shown in Figure 7, depending on the bias voltage applied to the device. At low voltage, we observe an initial rise and decay

https://doi.org/10.1021/acs.jpcc.3c04672
J. Phys. Chem. C 2023, 127, 21338−21350

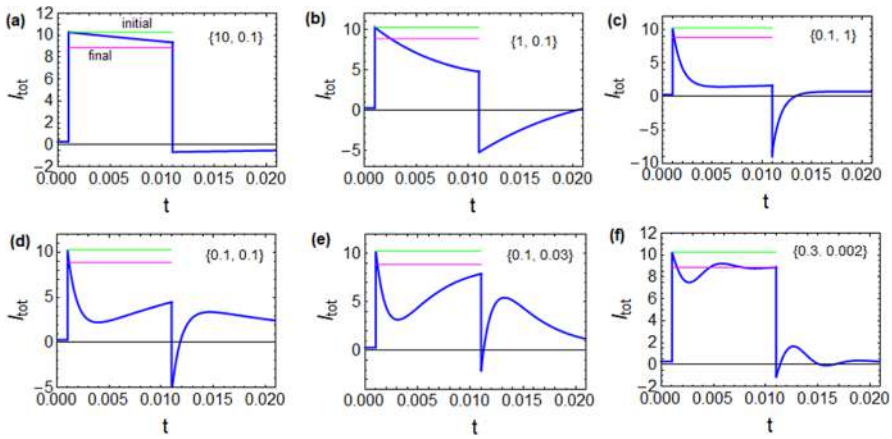

Figure 11. Model result of a transient voltage square pulse of value $V_1 = 0.1$ with duration $\Delta t = 0.05$ under constant illumination of photon flux $\Phi_1 = 10$ (blue). The green and purple reference lines are the initial and final currents. Parameters: $g_{b0} = 1$, $g_{a0} = 100$, $g_{b1} = 1$, $g_{a1} = 50$; $R_s = 0.01$; $\eta_{ph} = 0.2$; and $\{C_m, \tau_k\}$ as indicated. Note that the capacitor charging time $\tau_s = R_s C_m$.

of the current, while at higher voltage, there is a fast rise and subsequent slow rise of the current.

In the experiment, we hold the device at a stabilized current due to the applied voltage V_1 in the dark. Then the step of illumination of light flux Φ_1 is applied during the interval Δt.

We define $R_{a0} = R_a$ $(\Phi_1 = 0)$ and $R_{ab0} = R_{ab}$ $(\Phi_1 = 0)$. Consider the initial voltage occurring before the step of illumination

$$u_0(\Phi_{pre} = 0) = \frac{1}{1 + \frac{R_s}{R_{ab0}}} V_1 \tag{15}$$

According to model (2), we expect an instant response of the terms $(g_{b0} + g_{b1}\,\Phi_1)u$ and $\eta_{ph}\Phi_1$, while the term in x will take some time to get updated to $(g_{a0} + g_{a1}\,\Phi_1)u$ by eq 3. The current associated with the fast conduction modes, when the light pulse is applied, is

$$I_{in}(\Phi_{pre} = 0) = \frac{1}{1 + \frac{R_s}{R_{ab0}}}\left(\frac{1}{R_b} + \frac{1}{R_{a0}}\right) + \eta_{ph}\Phi_1 \tag{16}$$

In Figure 12a, we show a situation in which the time constant τ_s is fast compared to Δt, and the applied voltage is relatively large. The capacitor is charged rapidly, and the current rises instantaneously to the fast initial current (eq 16), as indicated by the green line in Figure 12a. Thereafter occurs the effect of the inductor that makes the current increase over the inductive time τ_k up to the stationary value indicated in the purple line. In Figure 12a, due to the large applied voltage, the photoconductance terms dominate, and the final current is larger than the fast current component. But at low voltage, the reverse situation occurs, as indicated in Figure 12b. Here, the signal rises toward the green line, while the capacitor is being charged, and the effect of the inductor makes the current decrease toward the purple line. If the inductor characteristic time τ_k is longer, then the peak takes a longer time to reach the equilibrium current, as shown in Figure 12c. These features are well observed in Figure 9, where the initial peak shape at low voltage is overcome. The main property is whether $I_{fin} < I_{in}$ that leads to the initial peak, since the initial current has to decrease toward the stationary value, or vice versa if $I_{fin} > I_{in}$, in which the initial current rises to the final value.

Figure 13 shows the effect of removing the inductive effect by setting very large R_a values. We note that the capacitive rise

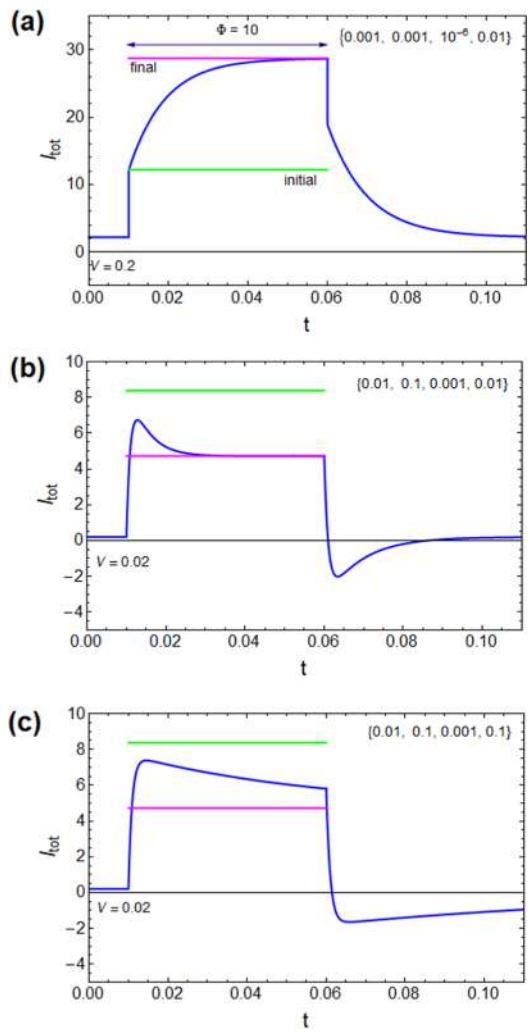

Figure 12. Model result of I−t curves under a photon flux square pulse of value $\Phi_1 = 10$ with duration $\Delta t = 0.05$ under constant applied voltage V_1 as indicated. The green and purple reference lines are the initial and final currents, respectively. Parameters: $g_{b0} = 1$, $g_{a0} = 10$, $g_{b1} = 1$, $g_{a1} = 10$; $\eta_{ph} = 0.8$; and $\{R_s, C_m, \tau_s, \tau_k\}$ as indicated.

starts from the first instant. The shape of the curve is independent of τ_k. Additional shapes according to the interplay

https://doi.org/10.1021/acs.jpcc.3c04672
J. Phys. Chem. C 2023, 127, 21338−21350

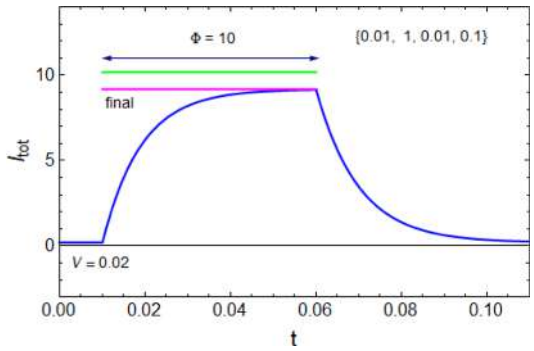

Figure 13. Model result of I−t curves under a photon flux square pulse of value $\Phi_1 = 10$ with duration $\Delta t = 0.05$ under constant applied voltage V_1 as indicated. The green and purple reference lines are the initial and final currents, respectively. Parameters: $g_{b0} = 1$, $g_{a0} = 0.001$, $g_{b1} = 1$, $g_{a1} = 0.001$; $\eta_{ph} = 0.8$; and $\{R_s, C_m, \tau_s, \tau_k\}$ as indicated.

of capacitive and inductive time constants at a high bias voltage are shown in Figure 14.

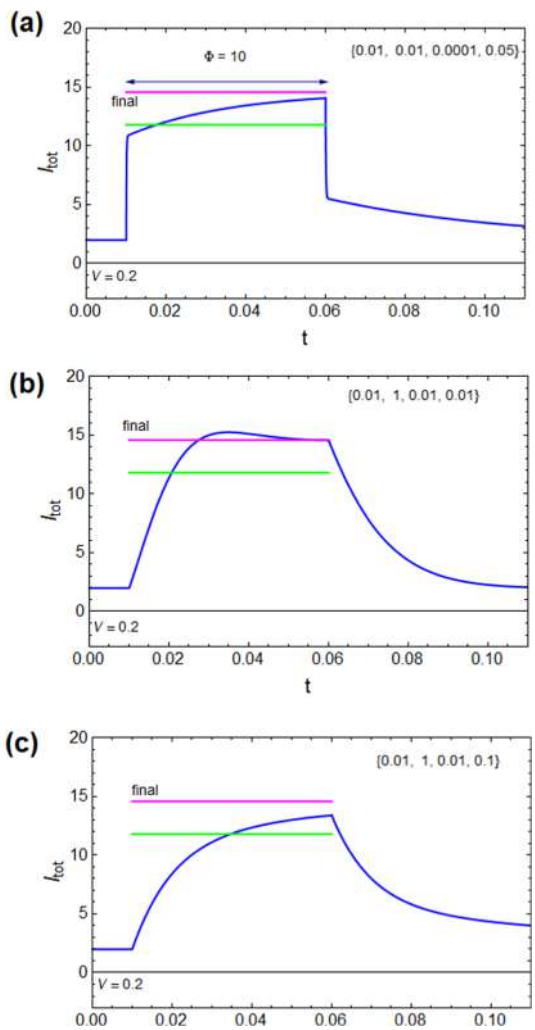

Figure 14. Model result of I−t curves under a photon flux square pulse of value $\Phi_1 = 10$ with duration $\Delta t = 0.05$ under constant applied voltage V_1 as indicated. The green and purple reference lines are the initial and final currents, respectively. Parameters: $g_{b0} = 1$, $g_{a0} = 10$, $g_{b1} = 1$, $g_{a1} = 10$; $\eta_{ph} = 0.8$; and $\{R_s, C_m, \tau_s, \tau_k\}$ as indicated.

We remark that the model explains the main transient photocurrent characteristics reported for solution-processed PDs. The capacitive or capacitive-inductive rise in Figures 12a and 13 accounts for the rise observed in halide perovskites at large applied bias. The initial peak and inductive decay of Figure 14b explain the many observations of the so-called "anomalous" initial overshoot[10] reported widely in organic and perovskite devices, as in Figure 2A.

We note that the shapes that rise from zero at the initial instant as in Figure 13 may not show the initial peak, as is the case in the transients of Figure 2C. This effect is purely capacitive, as commented before.

On the other hand, in the case of transients with an initial peak, when a large bias is applied, they will start the rise not from zero but from the value of I_{in}. This is observed in our measurements reported in Figure 9 upon modification of the applied potential. Our model well describes the evolution of this type of signal with an initial nonzero current, as shown in Figure 15.

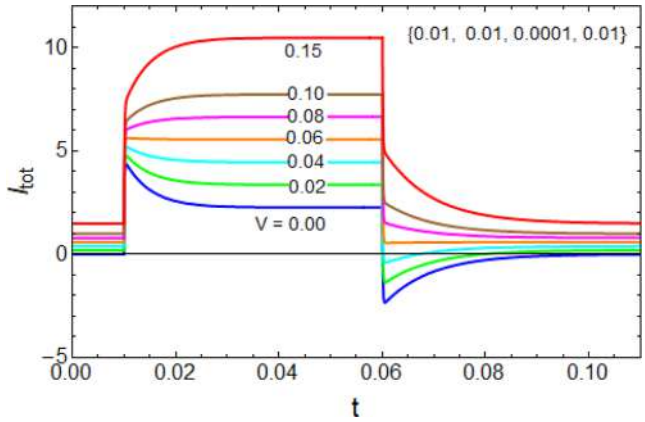

Figure 15. Model result of I−t curves under a photon flux square pulse of value $\Phi_1 = 10$ with duration $\Delta t = 0.05$ under constant applied voltage V_1 as indicated. Parameters: $g_{b0} = 1$, $g_{a0} = 10$, $g_{b1} = 1$, $g_{a1} = 10$; $\eta_{ph} = 0.5$; and $\{R_s, C_m, \tau_s, \tau_k\}$ as indicated.

This last result also allows us to understand the observations that occur when changing the thickness, as shown in Figure 1A.[16] This type of variation is consistently reported in the literature.[23] Since the applied voltage is maintained in the experiment, the longer devices contain a lower electrical field, which increases when reducing the thickness. Hence, the trend of Figure 15 is correspondingly observed in Figure 1A.

In this paper, we have used the basic capacitive and inductive processes indicated in Figures 4 and 5 as an effective aid for the interpretation of the transients. In many situations, a model such as eqs 1−3 and the related neuron-style models can be highly nonlinear and applied to a variety of techniques, e.g., the photo-CELIV mentioned before.[57−59]

This model gives insight into the dominant features of the transient signals of voltage and current, and it enables a classification of responses in terms of a few key parameters. More detailed models based on specific polarization and charge collection mechanisms can be applied to understand each of the main capacitive, transport, and inductive properties.[49]

https://doi.org/10.1021/acs.jpcc.3c04672
J. Phys. Chem. C 2023, 127, 21338−21350

6. CONCLUSIONS

Many types of organic and halide perovskite PDs show specific trends in the transient photocurrent in response to light pulse perturbation. The initial peak in current and subsequent stabilization are often observed under conditions affected by the slow dynamics of the system. It is also observed that a small applied voltage is equivalent to using a device geometry with a large channel of the active material. To explain these trends, a generic model is formed by using some basic physical characteristics of the PD response. The current is composed of a capacitive current, an instantaneous photocurrent, and an electrical field-dependent term with a photoconductance. An additional current is added with a slow relaxation time that produces the structure of an inductive photoresponse. These components are sufficient to explain the typical time transient observed in the literature and in our own measurements of $MAPbBr_3$ devices, in voltage and light pulses. We suggest that this type of model provides a useful general description of the temporal characteristics of the device with a small set of parameters. The model is particularly suitable for effectively categorizing experimental data. It can be extended to include additional internal processes and can serve as a benchmark for evaluating other models that adopt a more microscopic-molecular approach or employ drift-diffusion-recombination techniques.

■ AUTHOR INFORMATION

Corresponding Author

Juan Bisquert − *Institute of Advanced Materials (INAM), Universitat Jaume I, Castelló 12006, Spain;* orcid.org/0000-0003-4987-4887; Email: bisquert@uji.es

Authors

Cedric Gonzales − *Institute of Advanced Materials (INAM), Universitat Jaume I, Castelló 12006, Spain;* orcid.org/0000-0002-6550-2007

Antonio Guerrero − *Institute of Advanced Materials (INAM), Universitat Jaume I, Castelló 12006, Spain;* orcid.org/0000-0001-8602-1248

Complete contact information is available at: https://pubs.acs.org/10.1021/acs.jpcc.3c04672

Notes

The authors declare no competing financial interest.

■ ACKNOWLEDGMENTS

We thank the financial support from the Ministerio de Ciencia e Innovación of Spain (MICINN) project EUR2022-134045 and from the Generalitat Valenciana for the Grisolia Grant GRISOLIAP/2019/048.

■ REFERENCES

(1) García de Arquer, F. P.; Armin, A.; Meredith, P.; Sargent, E. H. Solution-processed semiconductors for next-generation photodetectors. *Nat. Rev. Mater.* **2017**, *2* (3), 16100.

(2) Ren, H.; Chen, J.-D.; Li, Y.-Q.; Tang, J.-X. Recent Progress in Organic Photodetectors and their Applications. *Advanced Science* **2021**, *8* (1), 2002418.

(3) Li, Z.; Gao, F.; Greenham, N. C.; McNeill, C. R. Comparison of the Operation of Polymer/Fullerene, Polymer/Polymer, and Polymer/Nanocrystal Solar Cells: A Transient Photocurrent and Photovoltage Study. *Adv. Funct. Mater.* **2011**, *21* (8), 1419−1431.

(4) Liu, Y.; Ji, Z.; Cen, G.; Sun, H.; Wang, H.; Zhao, C.; Wang, Z. L.; Mai, W. Perovskite-based color camera inspired by human visual cells. *Light: Sci. Appl.* **2023**, *12* (1), 43.

(5) Lin, Q.; Armin, A.; Burn, P. L.; Meredith, P. Filterless narrowband visible photodetectors. *Nat. Photonics* **2015**, *9* (10), 687−694.

(6) Jansen-van Vuuren, R. D.; Armin, A.; Pandey, A. K.; Burn, P. L.; Meredith, P. Organic Photodiodes: The Future of Full Color Detection and Image Sensing. *Adv. Mater.* **2016**, *28* (24), 4766−4802.

(7) Mei, L.; Huang, R.; Shen, C.; Hu, J.; Wang, P.; Xu, Z.; Huang, Z.; Zhu, L. Hybrid Halide Perovskite-Based Near-Infrared Photodetectors and Imaging Arrays. *Adv. Opt. Mater.* **2022**, *10* (9), 2102656.

(8) Li, C.; Wang, H.; Wang, F.; Li, T.; Xu, M.; Wang, H.; Wang, Z.; Zhan, X.; Hu, W.; Shen, L. Ultrafast and broadband photodetectors based on a perovskite/organic bulk heterojunction for large-dynamic-range imaging. *Light: Sci. Appl.* **2020**, *9* (1), 31.

(9) Li, G.; Wang, Y.; Huang, L.; Sun, W. Research Progress of High-Sensitivity Perovskite Photodetectors: A Review of Photodetectors: Noise, Structure, and Materials. *ACS Appl. Electron. Mater.* **2022**, *4* (4), 1485−1505.

(10) Hu, L.; Liu, X.; Dalgleish, S.; Matsushita, M. M.; Yoshikawa, H.; Awaga, K. Organic optoelectronic interfaces with anomalous transient photocurrent. *J. Mater. Chem. C* **2015**, *3* (20), 5122−5135.

(11) Lee, H. K.; Suh, T. S.; Choe, B. Y.; Shinn, K. S.; Cho, G.; Perez-Mendez, V. Transient photoconductive gain in a-Si:H devices and its applications in radiation detection. *Nucl. Instrum. Methods Phys. Res., Sect. A* **1997**, *399* (2−3), 324−334.

(12) Dou, L.; Yang, Y.; You, J.; Hong, Z.; Chang, W.-H.; Li, G.; Yang, Y. Solution-processed hybrid perovskite photodetectors with high detectivity. *Nat. Commun.* **2014**, *5* (1), 5404.

(13) Lin, Q.; Armin, A.; Lyons, D. M.; Burn, P. L.; Meredith, P. Low Noise, IR-Blind Organohalide Perovskite Photodiodes for Visible Light Detection and Imaging. *Adv. Mater.* **2015**, *27* (12), 2060−2064.

(14) Moseley, O. D. I.; Roose, B.; Zelewski, S. J.; Stranks, S. D. Identification and Mitigation of Transient Phenomena That Complicate the Characterization of Halide Perovskite Photodetectors. *ACS Appl. Energy Mater.* **2023**, DOI: 10.1021/acsaem.2c03453.

(15) Mahapatra, A.; Anilkumar, V.; Nawrocki, J.; Pandey, S. V.; Chavan, R. D.; Yadav, P.; Prochowicz, D. Transient Photocurrent Response in a Perovskite Single Crystal-Based Photodetector: A Case Study on the Role of Electrode Spacing and Bias. *Adv. Electron. Mater.* **2023**, *9* (8), 2300226.

(16) Gavranovic, S.; Pospisil, J.; Zmeskal, O.; Novak, V.; Vanysek, P.; Castkova, K.; Cihlar, J.; Weiter, M. Electrode Spacing as a Determinant of the Output Performance of Planar-Type Photodetectors Based on Methylammonium Lead Bromide Perovskite Single Crystals. *ACS Appl. Mater. Interfaces* **2022**, *14* (17), 20159−20167.

(17) Ding, J.; Gao, W.; Gao, L.; Lu, K.; Liu, Y.; Sun, J.-L.; Yan, Q. Unraveling the Effect of Halogen Ion Substitution on the Noise of Perovskite Single-Crystal Photodetectors. *J. Phys. Chem. Lett.* **2022**, *13*, 7831−7837.

(18) Wang, T.; Fang, T.; Li, X.; Xu, L.; Song, J. Controllable Transient Photocurrent in Photodetectors Based on Perovskite Nanocrystals via Doping and Interfacial Engineering. *J. Phys. Chem. C* **2021**, *125* (10), 5475−5484.

(19) Deng, H.; Yang, X.; Dong, D.; Li, B.; Yang, D.; Yuan, S.; Qiao, K.; Cheng, Y. B.; Tang, J.; Song, H. Flexible and Semitransparent Organolead Triiodide Perovskite Network Photodetector Arrays with High Stability. *Nano Lett.* **2015**, *15* (12), 7963−7969.

(20) Alwadai, N.; Haque, M. A.; Mitra, S.; Flemban, T.; Pak, Y.; Wu, T.; Roqan, I. High-Performance Ultraviolet-to-Infrared Broadband Perovskite Photodetectors Achieved via Inter-/Intraband Transitions. *ACS Appl. Mater. Interfaces* **2017**, *9* (43), 37832−37838.

(21) Ahmadi, M.; Wu, T.; Hu, B. A Review on Organic-Inorganic Halide Perovskite Photodetectors: Device Engineering and Fundamental Physics. *Adv. Mater.* **2017**, *29* (41), 1605242.

(22) Zhang, Y.; Liu, Y.; Yang, Z.; Liu, S. High-quality perovskite MAPbI3 single crystals for broad-spectrum and rapid response integrate photodetector. *J. Energy Chem.* **2018**, *27* (3), 722−727.
(23) Mahapatra, A.; Anilkumar, V.; Chavan, R. D.; Yadav, P.; Prochowicz, D. Understanding the Origin of Light Intensity and Temperature Dependence of Photodetection Properties in a MAPbBr3 Single-Crystal-Based Photoconductor. *ACS Photonics* **2023**, *10* (5), 1424−1433.
(24) Sutherland, B. R.; Johnston, A. K.; Ip, A. H.; Xu, J.; Adinolfi, V.; Kanjanaboos, P.; Sargent, E. H. Sensitive, Fast, and Stable Perovskite Photodetectors Exploiting Interface Engineering. *ACS Photonics* **2015**, *2* (8), 1117−1123.
(25) Gao, L.; Zeng, K.; Guo, J.; Ge, C.; Du, J.; Zhao, Y.; Chen, C.; Deng, H.; He, Y.; Song, H.; et al. Passivated Single-Crystalline CH3NH3PbI3 Nanowire Photodetector with High Detectivity and Polarization Sensitivity. *Nano Lett.* **2016**, *16* (12), 7446−7454.
(26) Chang, Y.; Wang, J.; Wu, F.; Tian, W.; Zhai, W. Structural Design and Pyroelectric Property of SnS/CdS Heterojunctions Contrived for Low-Temperature Visible Photodetectors. *Adv. Funct. Mater.* **2020**, *30* (23), 2001450.
(27) Chen, Z.; Cheng, Z.; Wang, J.; Wan, X.; Shu, C.; Tsang, H. K.; Ho, H. P.; Xu, J.-B. High Responsivity, Broadband, and Fast Graphene/Silicon Photodetector in Photoconductor Mode. *Adv. Opt. Mater.* **2015**, *3* (9), 1207−1214.
(28) Hernández-Balaguera, E.; Bisquert, J. Negative Transient Spikes in Halide Perovskites. *ACS Energy Lett.* **2022**, *7*, 2602−2610.
(29) Bisquert, J.; Guerrero, A. Chemical Inductor. *J. Am. Chem. Soc.* **2022**, *144*, 5996−6009.
(30) Gonzales, C.; Guerrero, A.; Bisquert, J. Transition from capacitive to inductive hysteresis: A neuron-style model to correlate I-V curves to impedances of metal halide perovskites. *J. Phys. Chem. C* **2022**, *126*, 13560−13578.
(31) Bisquert, J. Electrical Charge Coupling Dominates the Hysteresis Effect of Halide Perovskite Devices. *J. Phys. Chem. Lett.* **2023**, *14*, 1014−1021.
(32) Bisquert, J.; Bou, A.; Guerrero, A.; Hernández-Balaguera, E. Resistance transient dynamics in switchable perovskite memristors. *APL Mach. Learn.* **2023**, *1*, 036101.
(33) Munoz-Diaz, L.; Rosa, A. J.; Bou, A.; Sanchez, R. S.; Romero, B.; John, R. A.; Kovalenko, M. V.; Guerrero, A.; Bisquert, J. Inductive and Capacitive Hysteresis of Halide Perovskite Solar Cells and Memristors Under Illumination. *Front. Energy Res.* **2022**, *10*, 914115.
(34) Bisquert, J.; Guerrero, A. Dynamic Instability and Time Domain Response of a Model Halide Perovskite Memristor for Artificial Neurons. *J. Phys. Chem. Lett.* **2022**, *13*, 3789−3795.
(35) Kuehn, C. *Multiple Time Scale Dynamics*; Springer, 2015.
(36) Izhikevich, E. M. *Dynamical Systems in Neuroscience*; MIT Press, 2007.
(37) Hodgkin, A. L.; Huxley, A. F. A quantitative description of membrane current and its application to conduction and excitation in nerve. *J. Physiol.* **1952**, *117* (4), 500−544.
(38) Sakhatskyi, K.; John, R. A.; Guerrero, A.; Tsarev, S.; Sabisch, S.; Das, T.; Matt, G. J.; Yakunin, S.; Cherniukh, I.; Kotyrba, M.; et al. Assessing the Drawbacks and Benefits of Ion Migration in Lead Halide Perovskites. *ACS Energy Lett.* **2022**, *7* (10), 3401−3414.
(39) García-Batlle, M.; Deumel, S.; Huerdler, J. E.; Tedde, S. F.; Guerrero, A.; Almora, O.; Garcia-Belmonte, G. Mobile Ion-Driven Modulation of Electronic Conductivity Explains Long-Timescale Electrical Response in Lead Iodide Perovskite Thick Pellets. *ACS Appl. Mater. Interfaces* **2021**, *13* (30), 35617−35624.
(40) Alvarez, A. O.; Arcas, R.; Aranda, C. A.; Bethencourt, L.; Mas-Marzá, E.; Saliba, M.; Fabregat-Santiago, F. Negative Capacitance and Inverted Hysteresis: Matching Features in Perovskite Solar Cells. *J. Phys. Chem. Lett.* **2020**, *11* (19), 8417−8423.
(41) Ghahremanirad, E.; Bou, A.; Olyaee, S.; Bisquert, J. Inductive Loop in the Impedance Response of Perovskite Solar Cells Explained by Surface Polarization Model. *J. Phys. Chem. Lett.* **2017**, *8*, 1402−1406.
(42) Fabregat-Santiago, F.; Kulbak, M.; Zohar, A.; Vallés-Pelarda, M.; Hodes, G.; Cahen, D.; Mora-Seró, I. Deleterious Effect of Negative Capacitance on the Performance of Halide Perovskite Solar Cells. *ACS Energy Lett.* **2017**, *2* (9), 2007−2013.
(43) Jacobs, D. A.; Shen, H.; Pfeffer, F.; Peng, J.; White, T. P.; Beck, F. J.; Catchpole, K. R. The two faces of capacitance: New interpretations for electrical impedance measurements of perovskite solar cells and their relation to hysteresis. *J. Appl. Phys.* **2018**, *124*, 225702.
(44) Shen, H.; Jacobs, D. A.; Wu, Y.; Duong, T.; Peng, J.; Wen, X.; Fu, X.; Karuturi, S. K.; White, T. P.; Weber, K.; et al. Inverted Hysteresis in CH3NH3PbI3 Solar Cells: Role of Stoichiometry and Band Alignment. *J. Phys. Chem. Lett.* **2017**, *8* (12), 2672−2680.
(45) Ebadi, F.; Taghavinia, N.; Mohammadpour, R.; Hagfeldt, A.; Tress, W. Origin of apparent light-enhanced and negative capacitance in perovskite solar cells. *Nat. Commun.* **2019**, *10* (1), 1574.
(46) Moia, D.; Gelmetti, I.; Calado, P.; Fisher, W.; Stringer, M.; Game, O.; Hu, Y.; Docampo, P.; Lidzey, D.; Palomares, E.; et al. Ionic-to-electronic current amplification in hybrid perovskite solar cells: ionically gated transistor-interface circuit model explains hysteresis and impedance of mixed conducting devices. *Energy Environ. Sci.* **2019**, *12*, 1296−1308.
(47) Mora-Seró, I.; Dittrich, T.; Garcia-Belmonte, G.; Bisquert, J. Determination of spatial charge separation of diffusing electrons by transient photovoltage measurements. *J. Appl. Phys.* **2006**, *100*, 103705.
(48) Hu, L.; Jin, W.; Feng, R.; Zaheer, M.; Nie, Q.; Chen, G.; Qiu, Z.-J.; Cong, C.; Liu, R. Photovoltage Reversal in Organic Optoelectronic Devices with Insulator-Semiconductor Interfaces. *Materials* **2018**, *11*, 1530.
(49) Labram, J. G. Operating principles of zero-bias retinomorphic sensors. *J. Phys. D: Appl. Phys.* **2023**, *56* (6), 065105.
(50) Guerrero, A.; Bisquert, J.; Garcia-Belmonte, G. Impedance spectroscopy of metal halide perovskite solar cells from the perspective of equivalent circuits. *Chem. Rev.* **2021**, *121*, 14430−14484.
(51) Taukeer Khan, M.; Khan, F.; Al-Ahmed, A.; Ahmad, S.; Al-Sulaiman, F. Evaluating the Capacitive Response in Metal Halide Perovskite Solar Cells. *Chem. Rec.* **2022**, *22* (7), No. e202100330.
(52) Juarez-Perez, E. J.; Sanchez, R. S.; Badia, L.; Garcia-Belmonte, G.; Kang, Y. S.; Mora-Sero, I.; Bisquert, J.; Bisquert, J. Photoinduced giant dielectric constant in lead halide perovskite solar cells. *J. Phys. Chem. Lett.* **2014**, *5*, 2390−2394.
(53) Bisquert, J. Negative inductor effects in nonlinear two-dimensional systems. Oscillatory neurons and memristors. *Chem. Phys. Rev.* **2022**, *3*, 041305.
(54) Ghahremanirad, E.; Almora, O.; Suresh, S.; Drew, A. A.; Chowdhury, T. H.; Uhl, A. R. Beyond Protocols: Understanding the Electrical Behavior of Perovskite Solar Cells by Impedance Spectroscopy. *Adv. Energy Mater.* **2023**, *13* (30), 2204370.
(55) Berruet, M.; Pérez-Martínez, J. C.; Romero, B.; Gonzales, C.; Al-Mayouf, A. M.; Guerrero, A.; Bisquert, J. Physical model for the current-voltage hysteresis and impedance of halide perovskite memristors. *ACS Energy Lett.* **2022**, *7*, 1214−1222.
(56) Hernández-Balaguera, E.; Munoz-Diaz, L.; Bou, A.; Romero, B.; Ilyassov, B.; Guerrero, A.; Bisquert, J. Long-Term Potentiation Mechanism of Biological Postsynaptic Activity in Neuro-Inspired Halide Perovskite Memristors. *Neuromorphic Comput. Eng.* **2023**, *3*, 024005.
(57) Juška, G. Photo-CELIV technique for the investigations of charge carriers transport and recombination in the organic solar cells. *Renewable Energy and the Environment Optics and Photonics Congress, Eindhoven, 2012/11/11*; Optica Publishing Group: Eindhoven, 2012.
(58) Stephen, M.; Genevičius, K.; Juška, G.; Arlauskas, K.; Hiorns, R. C. Charge transport and its characterization using photo-CELIV in bulk heterojunction solar cells. *Polym. Int.* **2017**, *66* (1), 13−25.
(59) Lorrmann, J.; Badada, B. H.; Inganäs, O.; Dyakonov, V.; Deibel, C. Charge carrier extraction by linearly increasing voltage: Analytic

framework and ambipolar transients. *J. Appl. Phys.* **2010**, *108* (11), 113705.

(60) Liu, S.; Guan, J.; Yin, L.; Zhou, L.; Huang, J.; Mu, Y.; Han, S.; Pi, X.; Liu, G.; Gao, P.; Zhou, S. Solution-Processed Synaptic Memristors Based on Halide Perovskite Nanocrystals. *J. Phys. Chem. Lett.* **2022**, *13* (47), 10994−11000.

(61) Gonzales, C.; Guerrero, A.; Bisquert, J. Spectral properties of the dynamic state transition in metal halide perovskite-based memristor exhibiting negative capacitance. *Appl. Phys. Lett.* **2021**, *118*, 073501.

(62) Bisquert, J.; Guerrero, A.; Gonzales, C. Theory of Hysteresis in Halide Perovskites by Integration of the Equivalent Circuit. *ACS Phys. Chem. Au* **2021**, *1*, 25−44.

https://doi.org/10.1021/acs.jpcc.3c04672
J. Phys. Chem. C 2023, 127, 21338−21350